Planetary and Space Science 95 (2014) 11–24

Contents lists available at ScienceDirect

Planetary and Space Science

journal homepage: www.elsevier.com/locate/pss

The digital global geologic map of Mars: Chronostratigraphic ages, topographic and crater morphologic characteristics, and updated resurfacing history ☆

K.L. Tanaka [a,*], S.J. Robbins [b], C.M. Fortezzo [a], J.A. Skinner Jr. [a], T.M. Hare [a]

[a] U.S. Geological Survey, Astrogeology Science Center, 2255 N. Gemini Drive, Flagstaff, AZ 86001, USA
[b] University of Colorado, Boulder, CO, USA

ARTICLE INFO

Article history:
Received 1 October 2012
Received in revised form
7 March 2013
Accepted 14 March 2013
Available online 29 March 2013

Keywords:
Mars
Geologic mapping
Photogeology
Resurfacing
Chronology

ABSTRACT

A new global geologic map of Mars has been completed in a digital, geographic information system (GIS) format using geospatially controlled altimetry and image data sets. The map reconstructs the geologic history of Mars, which includes many new findings collated in the quarter century since the previous, Viking-based global maps were published, as well as other discoveries that were made during the course of the mapping using new data sets. The technical approach enabled consistent and regulated mapping that is appropriate not only for the map's 1:20,000,000 scale but also for its widespread use by diverse audiences. Each geologic unit outcrop includes basic attributes regarding identity, location, area, crater densities, and chronostratigraphic age. In turn, units are grouped by geographic and lithologic types, which provide synoptic global views of material ages and resurfacing character for the Noachian, Hesperian, and Amazonian periods. As a consequence of more precise and better quality topographic and morphologic data and more complete crater-density dating, our statistical comparisons identify significant refinements for how Martian geologic terrains are characterized. Unit groups show trends in mean elevation and slope that relate to geographic occurrence and geologic origin. In comparison with the previous global geologic map series based on Viking data, the new mapping consists of half the number of units due to simpler, more conservative and globally based approaches to discriminating units. In particular, Noachian highland surfaces overall have high percentages of their areas now dated as an epoch older than in the Viking mapping. Minimally eroded (i.e., pristine) impact craters ≥3 km in diameter occur in greater proportion on Hesperian surfaces. This observation contrasts with a deficit of similarly sized craters on heavily cratered and otherwise degraded Noachian terrain as well as on young Amazonian surfaces. We interpret these as reflecting the relatively stronger, lava-rich, yet less-impacted materials making up much of the younger units. Reconstructions of resurfacing of Mars by its eight geologic epochs using the Hartmann and Neukum chronology models indicate high rates of highland resurfacing during the Noachian (peaking at 0.3 km^2/yr during the Middle Noachian), modest rates of volcanism and transition zone and lowland resurfacing during the Hesperian (~0.1 km^2/yr), and low rates of mainly volcanic and polar resurfacing (~0.01 km^2/yr) for most of the Amazonian. Apparent resurfacing increased in the Late Amazonian (~0.03 km^2/yr), perhaps due to better preservation of this latest record.

Published by Elsevier Ltd.

1. Introduction

Geologic maps provide, in a historical context, fundamental syntheses of knowledge of the materials, landforms, and processes that characterize planetary surfaces. Global maps provide a unique, all-encompassing assessment of the spatial and temporal sequences of geologic events that dominated the surface of a particular planet. For Mars, the first global geologic map was produced on a photomosaic of 1–2 km/pixel Mariner 9 images at a 1:25,000,000 scale (Scott and Carr, 1978). Next, Viking Orbiter data having resolutions of 100 to 300 m/pixel were used to generate a series of three 1:15,000,000-scale maps (Scott and Tanaka, 1986; Greeley and Guest, 1987, Tanaka and Scott, 1987). From these maps, an eight-epoch chronostratigraphy was developed for Mars, which resulted in page-sized time-stratigraphic maps of the surface (Tanaka, 1986). The maps were then assembled and

* Corresponding author. Tel.: +1 928 556 7208; fax: +1 928 556 7014.
E-mail addresses: kgoto@perc.it-chiba.ac.jp, ktanaka@usgs.gov, travelgoro@gmail.com (K.L. Tanaka), Stuart.Robbins@colorado.edu (S.J. Robbins), cfortezzo@usgs.gov (C.M. Fortezzo), jskinner@usgs.gov (J.A. Skinner Jr.), thare@usgs.gov (T.M. Hare).

☆For submission to: Planetary and Space Science, Special Issue on Planetary Geology Field Symposium, Kitakyushu, Japan.

0032-0633/$ - see front matter Published by Elsevier Ltd.
http://dx.doi.org/10.1016/j.pss.2013.03.006

synthesized digitally, and estimates of the resurfacing rates were determined for each mean epoch age by geologic process for both Hartmann- and Neukum-based chronologies (Hartmann and Neukum, 2001; Ivanov, 2001; Neukum et al., 2001; Hartmann, 2005; Tanaka et al., 1988). These rates were later revised according to new age assignments to the epochs (Hartmann and Neukum, 2001). These studies indicated that the highest resurfacing rates on Mars occurred during the Middle Noachian, with an apparent resurgence of geologic resurfacing during the Early Hesperian, perhaps driven by widespread volcanism.

The new generation of Mars orbital topographic and imaging data constitutes a significant improvement in the quality and resolution of morphologic and imaging information that justified a major new global mapping effort. In particular, Mars Global Surveyor (MGS) Mars Orbiter Laser Altimeter (MOLA) data provide an unprecedented set of accurate topographic and morphologic data in the form of a digital elevation model at 1/128° resolution (463 m/pixel at the equator) (Smith et al., 2001). These data have supported significant new advances in geologic mapping at a global, 1:15,000,000 scale for the Martian northern plains (Tanaka et al., 2005). In addition, Mars Odyssey (ODY) Thermal Emission Imaging System (THEMIS) near-infrared (IR) day and night-time images (100 m/pixel) and Mars Reconnaissance Orbiter (MRO) Context Camera (CTX) images (5–6 m/pixel) have complemented the MOLA data in support of the new global geologic mapping. The THEMIS day IR images are generally more effective at revealing morphologic details than visual-range Viking images.

Advances in mapping approaches applied to Mars address how units should be identified, mapped, named, grouped, and colored (Skinner and Fortezzo (2013); Tanaka et al., 2005). Contact types and structures have been revisited as well. Blind photogeologic mapping tests of well-understood terrestrial sites with data sets that mimic altimetry and image data acquired by Mars spacecraft indicate how to optimally split and lump potential map units and how to determine the accuracy of topographic- and morphologic-based relative-age inferences (Tanaka et al., 2009; Skinner and Fortezzo, 2012). These analyses have optimized the methodologies that have been applied to geologic mapping of Mars at global scale. Thus, the mapping approach used in the Viking-based map series differs from that of the new map in a few important ways. First, many of the Viking-based units included formation names that applied to local and regional features, such as large volcanoes, that have been grouped in the new map. Second, some of the Viking-based units are geomorphic variations of what is otherwise the same material unit. Third, lava sequences in the vast Tharsis volcanic complex were divided by relative age, but the new mapping indicates that the surface flows are much more spatially and temporally mixed than previously appreciated, even though the same general trends in age are confirmed. This resulted again in some reduction in units. Finally, the new mapping approach emphasizes simplicity, and so there is a tendency to combine units if there is not a compelling reason to split them. Overall, the number of Viking-based units mapped is 88 and other areal, geomorphic features (e.g., small volcanoes, channel bars, mountains) number seven. In contrast, the new map has 44 units and no areal features.

Planetary geologic maps were originally drafted by hand, commonly on image mosaics or air-brushed shaded relief bases that were also produced manually. With the advent of digital mapping technologies, maps and map bases are generated and manipulated using software that has increased in capability and sophistication over time. In addition, scanning and digital drafting have enabled conversion of manually drafted geologic maps into digital formats, including geographic information system (GIS) shapefiles and geodatabases—currently the most advanced digital mapping approach.

Compiling and publishing geologic maps in a digital format has many advantages. Digital maps permit accurate spatial statistical measurement and calculation of map properties, such as the areas of map units and outcrops and the lengths and orientations of linear features and densities of linear and point features. Also, comparisons can be made with other, spatially co-registered datasets and thematic maps that relate to composition, topography, crater density, and other surface physical characteristics, as well as with previous mapping results. This has been the case in the application of the previous geologic map of Mars, which was published on three sheets at a 1:15,000,000 scale in Mercator and Polar Stereographic projections (Scott and Tanaka, 1986; Greeley and Guest, 1987, Tanaka and Scott, 1987). Later, the map was digitized and used to reconstruct the resurfacing history of Mars (Tanaka et al., 1988), and eventually renovated into a GIS format that registers more accurately with the current geodetic and topographic definition of Mars (Skinner et al., 2006).

In this paper, we summarize the methods and results of geospatial analyses that we conducted on the new global geologic map of Mars (Tanaka et al., in review). Derived thematic mapping products of Mars include (1) chronostratigraphy and (2) resurfacing for each major chronologic period (Noachian, Hesperian, and Amazonian) by unit type. We also combine the mapping and chronostratigraphic determinations in order to reconstruct the quantitative resurfacing history by epoch and model-dependent absolute ages. We present comparisons of mapping with global digital elevation and slope models and with impact crater morphologies determined for all craters >3 km in diameter. Results provide global statistics that assist with both characterizing map units and unit groups as well as with providing lithologic and geographic context to evaluate other geospatially registered information.

2. Digital map product

The new global geologic map of Mars at a 1:20,000,000 scale (Tanaka et al., in review) was drafted and produced in a geographic information system (GIS) using the Environmental Systems Research Institute, Inc. (v. 10.0, ®1980–2012, Redlands, CA) ArcGIS software package. The geologic map is registered to the Mars Global Surveyor Mars Orbiter Laser Altimeter (MOLA) global digital elevation model (DEM) at 463 m/pixel horizontal spacing at the equator constructed from ~600 million laser ranging measurements having accuracies of ~100 m in a horizontal position and ~1 m in radius (Neumann et al., 2001; Smith et al., 2001) and geodetically fixed using the currently accepted model of Mars (Seidelmann et al., 2002). Some interpolation occurs in the DEM in equatorial latitudes, where east-west gaps between altimetry shots reach a few kilometers or more in places, and in the polar regions above $\pm 87°$ latitudes, over which the spacecraft did not directly track. The mapping also relied heavily on morphologic and brightness observations from global mosaics of Mars Odyssey (ODY) mission's Thermal Emission Imaging System (THEMIS) daytime and nighttime infrared images at 100 m/pixel spatial resolution (Christensen et al., 2004; Edwards et al., 2011). In a few cases, critical landforms required for identification of units and contacts were too small to resolve on THEMIS images; in these cases, the mapping relied on Mars Reconnaissance Orbiter Context Camera (CTX) images (5–6 m/pixel) to locate contacts, which could in turn be located on THEMIS data.

Drafted unit contacts and line features consist of polylines—segmented lines of connected sequences of vertices (points). The mapping was mostly performed at the 1:5,000,000 scale (25% of the map's publication scale; Tanaka et al. (in review)) using a vertex spacing of 5 km, which sufficiently propagates the fidelity

of linework from mapping to publication scale without increasing file sizes with extraneous detail. We applied photogeologic mapping techniques similar to those described by Tanaka et al. (2005) and Tanaka and Fortezzo (2012) to identify and discriminate 44 geologic units (forming ~1300 outcrops) and about 10 linear feature types (~3500 individual features mapped) that document major types and episodes of material emplacement and modification.

Units are delineated by morphologic, brightness, and topographic characteristics interpreted to have arisen during a unit's primary emplacement (rather than from secondary resurfacing effects; e.g., tectonism and erosion). Contrary to previous global geologic maps of Mars, we employ the descriptor term "undivided" to describe several layered units (Apu, Hpu, AHtu, Htu, HNhu, and Nhu) that we feel have the potential for stratigraphic sub-division during the construction of larger-scale (i.e., more zoomed in) geologic maps. Units are delineated by relative age as governed by superposition relations and impact crater densities of type localities (Platz et al., in preparation) and are grouped into geographic (highland, lowland, transition, basin, polar, and apron) and lithologic (volcanic and impact) categories. Transition units specifically occur along the highland/lowland boundary as well as dissect highland areas. Basin units infill parts of Hellas, Argyre, and Utopia basins. Apron units commonly skirt Tharsis shields and massifs along the highland/lowland boundary and east of Hellas Planitia and form slide deposits in Valles Marineris.

Our method of delineating and organizing map units is similar to global and continental scale geologic maps of Earth, which also highlight geographic occurrence, lithology, and age. In the "Geological Map of the World" (Bouysee, 2009), onshore and offshore areas form the major unit groups, which are subdivided by lithology and in turn by chronostratigraphic age. The "Geological Map of North America" (Reed et al., 2005), groups units by major lithological groups (sedimentary, volcanic, plutonic, metamorphic, and undivided crystalline rock) and then by age.

Each map unit is assigned an age range according to the Martian chronostratigraphic periods (Noachian, Hesperian, and Amazonian) (Scott and Carr, 1978) that are subdivided into eight epochs (Early, Middle, and Late Noachian; Early and Late Hesperian, and Early, Middle, and Late Amazonian) (Tanaka, 1986), based on stratigraphic relations and crater-density determinations. Each epoch has crater-density defined boundaries that are fit to widely used crater production and chronology functions (Hartmann and Neukum, 2001; Ivanov, 2001; Neukum et al., 2001; Hartmann, 2005; Werner and Tanaka, 2011). Crater counts were obtained using two approaches. The first approach consisted of counts within selected "type" unit surfaces for craters as small as 100 m

Table 1
Total unit areas and cumulative crater densities, based on the crater database of Robbins and Hynek (2012a). Unit AHi areas were assimilated into inferred underlying units. Densities are no. per 10^6 km^2 and errors are (no.)$^{0.5}$ per 10^6 km^2.

Unit name	Unit symbol	Area (10^6 km^2)	*N*(1)	Error	*N*(2)	Error	*N*(5)	Error	*N*(16)	Error
Late Amazonian polar dunes	lApd	0.30	163.4	23.3	103.4	18.6	46.7	12.5	3.3	3.3
Middle Amazonian lowland	mAl	3.13	1544.9	22.2	489.5	12.5	121.0	6.2	23.3	2.7
Late Hesperian lowland	lHl	17.28	1573.5	9.5	512.4	5.4	109.7	2.5	23.8	1.2
Late Amazonian polar cap	lApc	0.70	14.3	4.5	11.5	4.1	10.0	3.8	7.2	3.2
Amazonian polar undivided	Apu	2.00	271.3	11.7	143.6	8.5	76.6	6.2	32.0	4.0
Amazonian polar	Ap	0.22	808.2	60.6	254.3	34.0	113.5	22.7	22.7	10.2
Hesperian polar	Hp	1.35	3378.2	50.0	997.4	27.2	233.6	13.1	62.1	6.8
Hesperian polar undivided	Hpu	0.03	465.5	116.4	436.4	112.7	87.3	50.4	0.0	0.0
Hesperian polar edifice	Hpe	0.28	795.4	53.6	412.2	38.6	162.7	24.3	32.5	10.8
Early Amazonian basin	eAb	0.54	1286.6	48.7	309.2	23.9	75.5	11.8	9.2	4.1
Late Hesperian basin	lHb	0.92	939.2	32.0	415.2	21.2	132.6	12.0	20.7	4.7
Early Hesperian basin	eHb	0.42	1649.2	62.6	535.5	35.7	188.0	21.2	38.1	9.5
Hesperian and Noachian basin	HNb	0.66	1361.1	45.5	583.3	29.8	203.6	17.6	53.2	9.0
Late Amazonian volcanic	lAv	3.43	551.8	12.7	203.9	7.7	72.5	4.6	19.5	2.4
Late Amazonian volcanic field	lAvf	0.31	192.7	24.9	96.4	17.6	35.3	10.7	9.6	5.6
Amazonian volcanic	Av	2.16	772.6	18.9	255.8	10.9	74.5	5.9	7.4	1.9
Amazonian and Hesperian volcanic	AHv	13.33	1303.3	9.9	339.1	5.0	85.2	2.5	16.4	1.1
Late Hesperian volcanic	lHv	2.47	2171.5	29.7	509.7	14.4	98.4	6.3	15.4	2.5
Late Hesperian volcanic field	lHvf	0.44	1670.2	61.6	402.18	30.3	111.5	15.9	15.9	6.0
Early Hesperian volcanic	eHv	6.24	2960.1	21.8	820.3	11.5	246.7	6.3	73.4	3.4
Late Noachian volcanic	lNv	2.45	2213.9	30.1	804.8	18.1	258.7	10.3	74.3	5.5
Amazonian volcanic edifice	Ave	0.82	457.7	23.6	97.4	10.9	15.8	4.4	0.0	0.0
Hesperian volcanic edifice	Hve	0.38	2230.0	76.4	568.0	38.6	175.4	21.4	28.8	8.7
Noachian volcanic edifice	Nve	0.21	2658.4	113.7	845.6	64.1	330.5	40.1	34.0	12.9
Late Amazonian apron	lAa	0.28	158.0	23.6	63.2	14.9	14.0	7.0	0.0	0.0
Amazonian apron	Aa	0.99	130.7	11.5	71.4	8.5	18.1	4.3	2.0	1.4
Amazonian and Noachian apron	ANa	0.38	1017.7	51.5	481.5	35.4	195.2	22.2	44.2	10.7
Amazonian and Hesperian transition undivided	AHtu	2.23	614.5	16.6	230.7	10.2	62.8	5.3	6.7	1.7
Hesperian transition undivided	Htu	0.75	2262.8	54.8	608.4	28.4	176.3	15.3	37.1	7.0
Late Hesperian transition	lHt	2.40	1950.2	28.5	549.7	15.1	160.6	8.2	33.3	3.7
Early Hesperian transition	eHt	3.95	2715.1	26.2	848.2	14.7	238.7	7.8	50.9	3.6
Hesperian transition	Ht	0.91	1191.6	36.2	479.5	22.9	184.3	14.2	66.9	8.6
Hesperian transition outflow	Hto	1.35	1868.6	37.1	481.4	18.9	130.7	9.8	32.5	4.9
Hesperian and Noachian transition	HNt	3.15	2557.4	28.5	906.7	17.0	328.0	10.2	99.6	5.6
Hesperian and Noachian highland undivided	HNhu	1.07	3125.4	54.1	1185.5	33.3	379.5	18.9	109.6	10.1
Noachian highland undivided	Nhu	1.65	1667.3	31.7	504.1	17.4	148.5	9.5	39.2	4.9
Early Hesperian highland	eHh	1.89	2730.9	38.0	727.6	19.6	181.8	9.8	32.3	4.1
Late Noachian highland	lNh	8.98	3646.9	20.1	1183.8	11.5	385.3	6.5	116.0	3.6
Middle Noachian highland	mNh	34.80	4172.3	11.0	1487.1	6.5	581.1	4.1	177.4	2.3
Early Noachian highland	eNh	15.33	3877.3	15.9	1481.7	9.8	665.4	6.6	249.2	4.0
Nochian highland edifice	Nhe	0.22	3894.6	132.9	1459.9	81.4	702.8	56.4	172.3	27.9
Middle Noachian highland massif	mNhm	1.97	2669.1	36.8	1134.5	24.0	468.7	15.4	147.3	8.6
Early Noachian highland massif	eNhm	1.98	2707.9	37.0	1231.9	24.9	598.3	17.4	217.9	10.5

using Mars Express' High Resolution Stereo Camera (12.5–25 m/pixel) and CTX images using the Cratertools ArcGIS add-on and modeling ages with the Craterstats software tool (Michael and Neukum, 2010; Kneissl et al., 2011). The Craterstats tool permits extraction of resurfacing ages where craters in certain diameter ranges represent younger stages of geologic activity—in some cases these provide an emplacement age of a unit, which might also display a population of older, larger partly buried craters. This approach and its results are described in detail in Platz et al. (in preparation). A second approach to crater counting involved the intersection of the geologic map units with the global crater database of Robbins and Hynek (2012a), which documents the location, diameter, and other morphologic attributes of $>380{,}000$ craters larger than 1 km in diameter; this second approach is described herein.

3. Digital analysis of the global geologic map of Mars

We extracted and derived quantitative data from the new digital global map of Mars in order to help characterize physical and temporal aspects of the map units (and unit groups) by merging it with a global crater database and elevation and slope data. In addition, we make quantitative comparisons with the Viking-based geologic mapping to show the degree to which mapping interpretations have changed.

3.1. Distribution of map units by group and period

We intersected the unit mapping with the Robbins and Hynek (2012a) crater database of Mars and calculated cumulative crater densities for diameters larger than 1, 2, 5, and 16 km for each unit (Table 1). Those values were used to define epoch boundaries by Tanaka (1986), which was recently refined for single crater diameter intercepts of crater production size-frequency distributions at 1, 2, 5, and 16 km (Werner and Tanaka, 2011). Crater densities were also derived for individual outcrops using the same database, and those values were used as part of the evaluation of unit assignment to the outcrop, particularly if stratigraphic position determinations from mapping and unit morphologic discriminators were absent or weakly represented. In addition, crater counts down to smaller diameters for unit type areas and areas of special interest were performed for more detailed and rigorous crater-dating analysis (Platz et al., in preparation). In order to include larger, relatively pristine craters in the crater counts that are mapped as the Amazonian and Hesperian impact unit (AHi), a special revised unit map was constructed wherein unit AHi was removed and replaced by units inferred to underlie them based on surrounding units and topographic relationships indicative of buried contacts.

Some units span intervals involving multiple epochs. As such, we applied six additional designations for age (Amazonian, Hesperian, Noachian, Amazonian and Hesperian, Hesperian and Noachian, and Amazonian and Noachian). The unit information is displayed in thematic map figures by assigned unit ages (Fig. 1) and by coverage for each chronologic period and unit group (Fig. 2).

The Noachian map (Fig. 2A) shows the dominance of ancient highland terrain on Mars with relatively minor volcanic, basin, lowland materials. Exposed Hesperian rocks (Fig. 2B) illustrate infilling of the northern lowlands and large impact basins, accumulation of the earliest polar deposits, and growth of the Tharsis and Elysium volcanic rises. Parts of the highland-lowland transition zone retreated and were covered by sediments, and canyons and chaotic terrain formed by tectonism, incision, and collapse in Valles Marineris and nearby highland areas (also mapped as transition units). The Amazonian map (Fig. 2C) shows continued volcanism in the Tharsis and Elysium regions and local mass-wasting and accumulation of sediments along the highland-lowland transition region. Also, sedimentary aprons formed around Olympus Mons and Tharsis Montes. Remnants of a Middle Amazonian lowland unit and other basin and volcanic materials cover large patches of the northern plains. The polar plateaus largely formed in the Amazonian. Scattered Hesperian and Amazonian impact craters dot the highland landscape (Fig. 2B and C).

3.2. Elevation and slope of map units

The map units in large part are defined by their geographic occurrence, topographic form, and morphology, which to some degree relate to their elevation and slope characteristics. Mean unit surface elevations and their standard deviations provide a relative indicator of their topographic and geographic character. The elevation and slope data for each unit are summarized in Table 2. Basin units, which dominate the floors of Hellas, Argyre, and Utopia basins, are the lowest units, joined also by lowland and other units occurring predominantly within the north polar basin. Other relatively low units include volcanic and transition units in lowland plains near the highland-lowland boundary. Highland massif units making up the rims of Hellas, Argyre, and Isidis basins occur near the planetary datum. Other highland units have

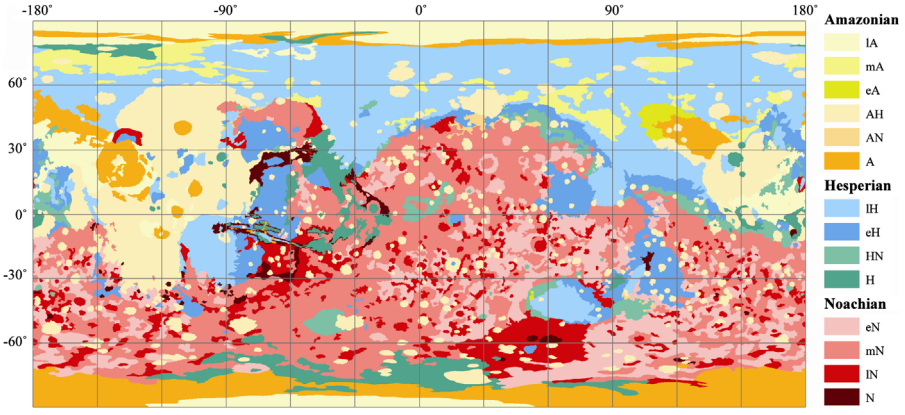

Fig. 1. Chronostratigraphic map of Mars showing surfaces of common age ranges. Unit abbreviations: A, Amazonian; H, Hesperian; N, Noachian; l, Late; m, Middle, e, Early. Note that some units cover single epochs (e.g., eN), others cover entire periods (N, H, A), and a few cover multiple periods (HN, AN, AH). Equirectangular projection, 30° grid.

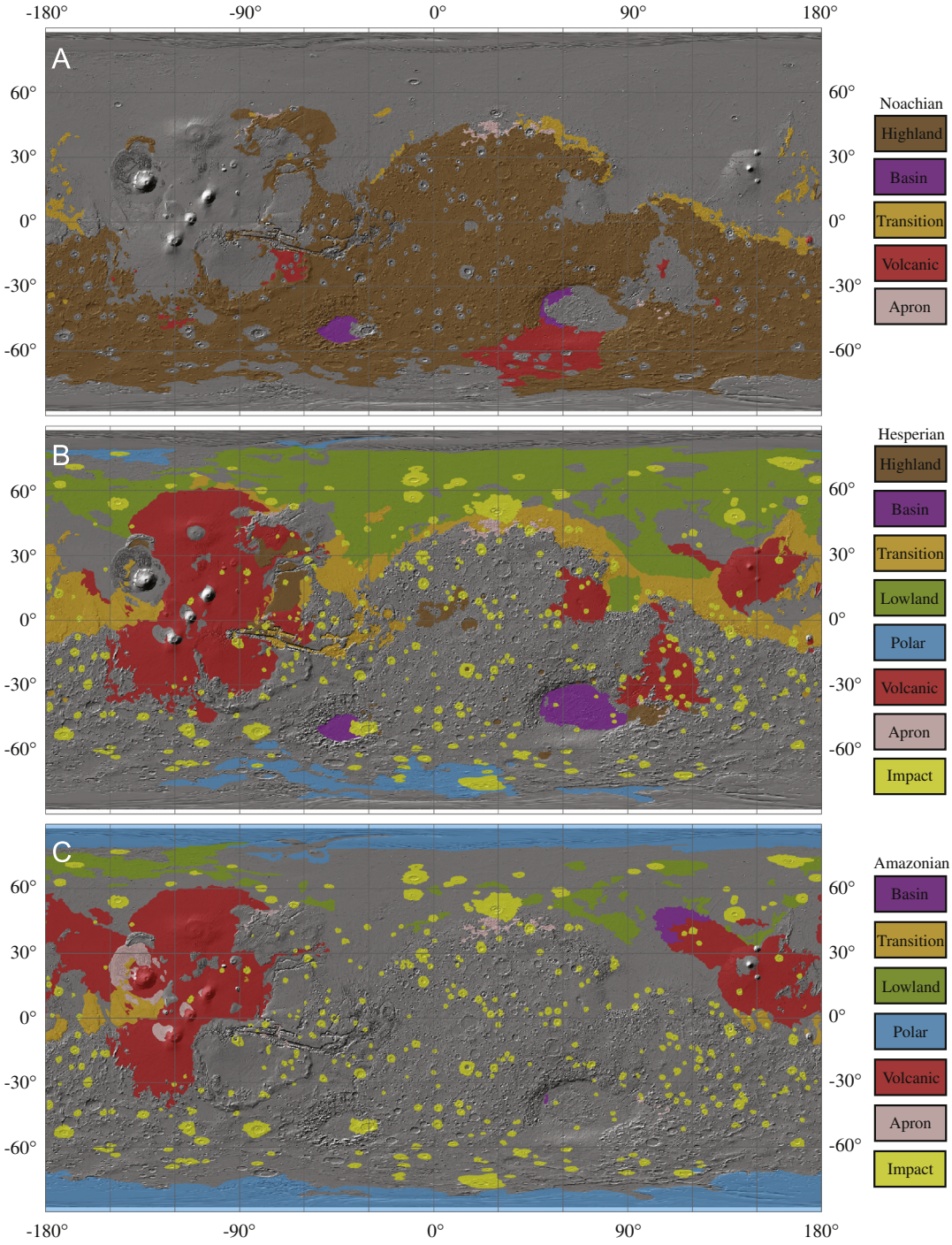

Fig. 2. Unit groups on Mars by period; (A) Noachian, (B) Hesperian, and (C) Amazonian. Some units span two periods. Base map is a MOLA shaded relief digital elevation model (128 pixels/deg) overlain by a global THEMIS daytime infrared mosaic (100 m/pixel). Equirectangular projection, 30° grid.

average heights <1000 m above datum, except the rugged Early Noachian highland unit, which stands at ~1500 m elevation. Among the highest standing units are volcano edifice, highland edifice, volcanic field, Hesperian volcanic, and two of the polar units (Apu and Hp).

We used the MOLA DEM cell size (1/128°; 463 m at the equator) as the standard horizontal distance over which slopes are measured. (Individual MOLA tracks have been used previously to measure slopes at 0.6, 2.4, and 19.2 km length scales, which are multiples of laser shot-point spacings (Kreslavsky and Head, 2000)) Overall, most units are modestly sloping, with 16 having mean slopes of $<1°$ and another 16 having slopes between 1° and 2°. All units $<1°$ are Amazonian or Hesperian and occur almost exclusively in the northern plains. The steepest units, having mean slopes of 3° to 7°, include edifice, massif, apron, undivided (i.e., exposed scarps with layering), and Hesperian transition (i.e., chaotic terrain material) units; their high slopes are likely to have resulted primarily due to volcanic construction and/or slope-related erosional processes. These results are consistent with results of Kreslavsky and Head (2000) for their mapping of a

Table 2
Mean elevation and slope statistics for Mars global map units, in order of mean elevation.

Unit	Mean elevation (m)	Elevation standard deviation (m)	Mean slope (deg)	Slope standard deviation (deg)
lHb	−6515	332	1.70	1.50
eHb	−6265	273	0.88	1.10
eAb	−4993	353	0.40	0.77
Hpu	−4653	421	0.69	1.28
lApd	−4650	263	0.57	0.49
HNb	−4401	1971	1.37	1.58
lHl	−4347	458	0.42	0.74
mAl	−4206	409	0.49	0.70
Av	−4197	354	0.44	0.85
lHt	−3365	829	0.74	1.90
Hto	−3214	1158	0.98	2.41
eHt	−3200	549	1.12	2.07
lAv	−3065	1231	0.38	1.42
Ht	−2916	1196	6.90	6.37
Hpe	−2700	3175	1.23	1.57
ANa	−2454	1322	3.82	4.83
HNt	−2419	905	3.39	4.01
Htu	−2161	1112	3.23	4.83
lApc	−1949	2672	0.84	1.55
Aa	−1795	1215	5.33	4.86
AHtu	−1514	1360	1.38	1.61
HNhu	−1376	1322	1.48	2.31
AHi	−804	2687	2.14	3.08
Nhu	−225	2768	5.80	8.20
eNhm	−188	1746	3.26	3.53
mNhm	103	1282	4.43	4.48
lNv	270	2345	1.03	1.60
eHh	294	1480	1.39	3.00
mNh	578	1650	1.89	2.74
lNh	681	1766	1.13	2.02
AHv	785	2856	0.69	1.47
Apu	807	2984	0.76	1.29
Hp	1280	345	0.78	1.20
eHv	1284	1591	1.21	2.46
Nve	1299	1121	1.70	2.21
Hve	1419	2803	2.96	3.34
eNh	1481	1225	2.47	3.13
Ap	1689	419	1.83	2.26
lAvf	2187	4765	0.54	1.63
lHvf	2478	2755	0.98	2.29
Nhe	2926	1473	3.16	3.14
lAa	3880	1890	1.95	2.43
lHv	4235	2280	1.49	3.59
Ave	7552	5299	3.73	3.87

0.6 km slope scale, and the longer slope baselines that they also measured provide for additional capability for discrimination of kilometer-scale roughness characteristics among volcanic, lowland, polar, and other units.

3.3. Comparison with viking-based units

Given that both the Viking- and post-Viking-based geologic maps of Mars are in GIS format, it is a straightforward exercise to spatially intersect the maps and compare the two sets of units (Tables 3 and 4). However, understanding the results is less than straightforward. Here we compare units by post-Viking unit group type to reveal what changes have occurred in broad terms.

The polar and lowland unit groups correspond well with similar Viking units, except that the Middle Amazonian lowland unit (mAl) is newly recognized (Skinner et al., 2012) and has no Viking map counterpart. This is true also for the post-Viking volcanic units, except for the Noachian volcanic units (lNv and Nve), because the Viking-based mapping did not recognize any Noachian volcanic unit (although some were previously identified as Hesperian volcanic units). Also, most of the lava flows in Daedalia Planum are now mapped as a single unit—the Amazonian and Hesperian volcanic unit (AHv)—given that clear, consistent geomorphic and stratigraphic boundaries are not observed; previously, the flows were divided into several units based on mean crater age and local overlap relations observed in Viking images (Fig. 3). The older basin units in the post-Viking map correspond largely with the Hellas assemblage units in the Viking mapping, although with some significant changes in unit boundaries (Fig. 4). The youngest basin unit's (eAb) largest outcrop in Utopia Planitia was not recognized as a separate unit distinct from materials more proximal to Elysium Mons in the Viking map.

The post-Viking map's impact unit (AHi), widespread on Mars, overlaps only 35% with its Viking equivalent (mapped as unit c by Scott and Tanaka (1986), Greeley and Guest (1987), and Tanaka and Scott (1987)). Each map stipulates that craters >100 km across are mapped, and comparison of the two maps shows differences in which craters are mapped and also significant differences in how crater margins have been drawn (Figs. 3 and 4). This difference is also consistent with what Robbins and Hynek (2012a) found when creating a new global Mars crater database: post-Viking data permit the identification of ~10% more craters with diameters >100 km than Barlow (1988) identified when using Viking data.

Post-Viking highland–lowland transition units share some equivalent kinds of units with the Viking maps. The transition undivided units (AHtu and Htu) are layered and deeply wind-eroded sequences located along the highland-lowland boundary between the Elysium and Tharsis regions. In the Viking-based maps, the bulk of these units were mapped as lower, middle, and upper members of the Medusae Fossae Formation (units Aml, Amm, and Amu). We were unable to consistently and confidently identify three stratigraphically distinct, sequential units as indicated in the previous Viking-based geologic maps. However, we did identify a consistently mappable separation between upper and lower sections of the formation, which we interpret as a major unconformity. This unconformity is marked by a higher density of craters, wrinkle ridges, and locally inverted channels (as described by Burr et al. (2009)). The older sequence is Hesperian in age, although a high degree of unit erosion lessens temporal constraint. The post-Viking Hesperian transition unit (Ht) corresponds mostly with Viking mapping of chaotic (unit Hcht) and channel (unit Hch) materials (Table 3), which occur in dissected and collapsed terrains between Valles Marineris and Chryse Planitia. However, we observe that the degree of chaos development in these terrains is greater than previously recognized. The post-Viking Hesperian transition outflow unit (Hto) was previously mapped as channel (Hch), floodplain (Hchp), and other plains materials mostly of Hesperian age. Materials along the highland-lowland boundary identified in the post-Viking map as transition units include a mixture of eroded Noachian highland materials embayed by Hesperian plains materials (unit HNt) as well as discrete Hesperian plains units (eHt and lHt); these surfaces were previously shown in the Viking maps as undivided (HNu), knobby (Apk), and various plains units of Noachian to Amazonian age.

In the post-Viking map, apron units are interpreted as slope-forming materials generally resulting from mass-wasting and mass-flow processes, thus emphasizing a genetic interpretation. This map delineates an Amazonian and Noachian apron unit (ANa), which includes degraded highland materials (and associated plains) along the highland–lowland boundary north of Arabia Terra and some massif slopes northeast of Hellas basin, whereas the Amazonian apron unit (Aa) consists of the Olympus Mons aureoles and Valles Marineris landslides. The Viking maps represented these units mostly as slide (As) and undivided (HNu) materials and aureole members (Aoa_{1-4}) of the Olympus Mons Formation.

Table 3
Percentages of Viking-based map units (from digital map of Skinner et al. (2006) for each unit in the new mapping by Tanaka et al. (in review); values < 5% not shown.

Unit name	Unit symbol	Area (10^6 km^2)	I-1802 units (% intersect)
Late Amazonian polar dunes	**lApd**	0.30	**Adl** (66), **Adc** (28), **Am** (5)
Middle Amazonian lowland	**mAl**	2.99	**Am** (21), **Hvk** (20), **Hvm** (18), **Apk** (14), **Hvg** (6), **HNu** (6)
Late Hesperian lowland	**lHl**	15.96	**Hvk** (31), **Hvm** (16), **Aa$_1$** (11), **Hvg** (11), **Hvr** (8), **Apk** (6), **Am** (5)
Amazonian and Hesperian impact	**AHi**	7.87	**cs** (35), **Npl$_1$** (17), **Hr** (7), **Npld** (7), **Npl$_2$** (5)
Late Amazonian polar cap	**lApc**	0.70	**Api** (82), **Apl** (18)
Amazonian polar undivided	**Apu**	2.00	**Apl** (79), **Api** (10)
Amazonian polar	**Ap**	0.22	**HNu** (53), **Hdl** (24), **Hdu** (14), **Am** (5)
Hesperian polar	**Hp**	1.22	**Hdu** (53), **Hdl** (21), **HNu** (9), **Npl$_2$** (7)
Hesperian polar undivided	**Hpu**	0.03	**Apl** (52), **Am** (32), **Hvg** (14)
Hesperian polar edifice	**Hpe**	0.26	**Am** (55), **HNu** (14), **Api** (9), **Nplh** (5)
Early Amazonian basin	**eAb**	0.54	**Ael$_3$** (77), **Hvg** (9)
Late Hesperian basin	**lHb**	0.91	**Hh$_3$** (69), **Hh$_2$** (14), **Ah$_8$** (13)
Early Hesperian basin	**eHb**	0.39	**Hh$_2$** (77), **Hh$_3$** (21)
Hesperian and Noachian basin	**HNb**	0.59	**Hh$_2$** (28), **Nple** (27), **Hpl$_3$** (20), **Hr** (8), **Ah$_7$** (7), **Ah$_6$** (5)
Late Amazonian volcanic	**lAv**	3.40	**Aa$_3$** (34), **Achu** (22), **Aop** (9), **Aa$_4$** (7), **Ael$_1$** (6), **Aps** (6)
Late Amazonian volcanic field	**lAvf**	0.31	**Aps** (21), **At$_5$** (18), **At$_6$** (16), **AHcf** (11), **Aop** (11), **Apk** (10), **Achu** (7)
Amazonian volcanic	**Av**	2.09	**Ael$_3$** (37), **Aa$_4$** (18), **Aa$_3$** (13), **Aa$_1$** (7)
Amazonian and Hesperian volcanic	**AHv**	13.16	**At$_5$** (21), **Ael$_1$** (15), **Hal** (13), **At$_4$** (9), **Aam** (8), **AHt$_3$** (6), **At$_6$** (5)
Late Hesperian volcanic	**lHv**	2.38	**Hsu** (36), **Hsl** (20), **Hf** (15), **Nf** (9), **Hr** (7)
Late Hesperian volcanic field	**lHvf**	0.44	**Hsu** (26), **Ael$_1$** (24), **Htu** (15), **AHcf** (8), **Ht$_2$** (7), **Htm** (6)
Early Hesperian volcanic	**eHv**	5.77	**Hr** (42), **Hs** (22), **Hpl$_3$** (8), **Nf** (5)
Late Noachian volcanic	**lNv**	2.22	**Hr** (49), **Had** (19), **Nplr** (7), **Hh$_2$** (5)
Amazonian volcanic edifice	**Ave**	0.82	**Aos** (43), **AHt$_3$** (37), **Aau** (15)
Hesperian volcanic edifice	**Hve**	0.38	**v** (25), **AHh** (23), **Ael$_2$** (23), **Ael$_1$** (9), **Hhet** (6), **AHa** (5), **AHat** (5)
Noachian volcanic edifice	**Nve**	0.21	**Hr** (22), **AHt** (21), **Had** (20), **Hap** (13), **AHa** (13)
Late Amazonian apron	**lAa**	0.28	**As** (87), **AHt$_3$** (5)
Amazonian apron	**Aa**	0.99	**Aoa$_1$** (40), **Aoa$_4$** (24), **Aoa$_3$** (13), **Aoa$_2$** (7), **Ae** (5)
Amazonian and Noachian apron	**ANa**	0.37	**As** (53), **HNu** (9), **Hr** (7), **Hch** (7)
Amazonian and Hesperian transition undivided	**AHtu**	2.19	**Amu** (43), **Amm** (26), **Aml** (15)
Hesperian transition undivided	**Htu**	0.74	**Aml** (28), **Amm** (23), **Hvl** (11), **Avf** (7), **Achu** (7), **Apk** (6), **HNu** (5), **Npl$_2$** (5)
Late Hesperian transition	**lHt**	2.34	**Aa$_1$** (29), **Aps** (20), **Hr** (13), **Apk** (12)
Early Hesperian transition	**eHt**	3.67	**Hr** (40), **AHpe** (11), **Apk** (10), **Aa$_1$** (8), **Aps** (7), **HNu** (7), **Npld** (5)
Hesperian transition	**Ht**	0.91	**Hcht** (58), **Hch** (14), **Npl$_2$** (7)
Hesperian transition outflow channel	**Hto**	1.28	**Hch** (33), **Hchp** (33), **Aa$_1$** (19), **Hr** (12)
Hesperian and Noachian transition	**HNt**	2.88	**HNu** (48), **Apk** (13), **Aa$_1$** (8), **Npl$_2$** (5)
Hesperian and Noachian highland undivided	**HNhu**	1.00	**Npl$_2$** (47), **Ah$_5$** (21), **Nple** (6), **Hpl$_3$** (5)
Noachian highland undivided	**Nhu**	1.60	**Hch** (24), **HNu** (20), **Hchp** (14), **Npl$_1$** (8), **Npl$_2$** (5), **Hr** (5), **Nf** (5)
Early Hesperian highland	**eHh**	1.80	**Hr** (70), **Hf** (7), **Npl$_2$** (6)
Late Noachian highland	**lNh**	8.39	**Hr** (29), **Hpl$_3$** (16), **Npl$_2$** (12), **Npl$_1$** (10), **Nplr** (7), **Npld** (6)
Middle Noachian highland	**mNh**	32.19	**Npl$_1$** (32), **Npld** (22), **Npl$_2$** (14), **Hr** (8), **Nplr** (7)
Early Noachian highland	**eNh**	15.96	**Npl$_1$** (36), **Npld** (30), **Nplr** (8), **Npl$_2$** (5)
Noachian highland edifice	**Nhe**	0.22	**Npl$_1$** (22), **v** (19), **Nf** (16), **Nb** (10), **Nplh** (7), **Npl$_2$** (6), **Hr** (5)
Middle Noachian highland massif	**mNhm**	1.87	**Nplh** (57), **Hpl$_3$** (15), **Npld** (11), **Npl$_2$** (6)
Early Noachian highland massif	**eNhm**	1.94	**Nh$_1$** (67), **Nm** (11), **Npl$_2$** (11)

The most discrepant mapping between the post-Viking- and Viking-based geologic maps occurs within highland units (Fig. 4), where there is a net shift in the amount of area assigned to older epochs in the new mapping (Table 3). The youngest, post-Viking, Early Hesperian highland unit (eHh) corresponds closely with Early Hesperian units (Hr and Hf) of the Viking mapping. The post-Viking Hesperian and Noachian highland undivided unit (HNhu) includes materials forming interior layered deposits of VallesMarineris, deposits of MeridianiPlanum, and scattered crater fill located mostly north and west of Hellas basin as well as forming the Gale crater mound (formally named Aeolis Mons). Post-Viking unit HNhu corresponds to somewhat equivalent but diverse Late Noachian to Early Amazonian units (Hvl, Npl$_2$, Avf, HNu, and s) in the previous mapping. The post-Viking Late Noachian highland unit (lNh) largely forms thin deposits infilling shallow intra- and inter-crater basins in the Martian cratered highlands. However, the Viking mapping considered nearly half of the unit to be Early Hesperian (Hr and Hpl$_3$)—and some of it Noachian—in age (Npl and Nf units). The Middle Noachian highland unit in the post-Viking map dominates the highlands of Mars and covers a total area similar to that of its Viking-based, Middle Noachian equivalents (Npl$_1$ and Npld). However, this is misleading because about a quarter of the area of unit mNh overlaps Late Noachian and Early Hesperian Viking-based units (Npl$_2$, Nplr, and Hr). The post-Viking Middle Noachian highland massif unit (mNhm) forms the rugged rims of Argyre and Isidis basins, considered largely Early Noachian (Nplh) in the previous mapping. The post-Viking Early Noachian highland unit (eNh) is more than half the surface area of unit mNh and forms much of the higher annulus to Hellas basin, but in the Viking mapping it was nearly all mapped as Middle Noachian units (Npl$_1$, Npld, and Nplr). Post-Viking Noachian highland undivided (Nhu) and edifice (Nhe) units for the most part were not identified in the Viking mapping and thus correspond with diverse Noachian and Hesperian units. The older age assignments in the post-Viking map reflect both mapping results, where MOLA topographic data commonly show how older units tend to be more rugged and higher standing, whereas Viking images commonly did not convey topography and morphology as precisely.

3.4. Chronostratigraphic controls on crater morphology

Robbins and Hynek (2012b) conducted a density analysis of $D \geq 5$ km impact crater and ejecta preservation as a function of terrain chronostratigraphic age using the Viking-based geologic maps. This analysis was to determine whether impact feature preservation was a strict function of terrain age or if other factors were involved. On a body with an atmosphere and more recent

Table 4
Percentages of new map units of Tanaka et al. (in review) for each unit in the Viking-based map units (from digital map of Skinner et al. (2006); values < 5% not shown. Units organized as in Tanaka et al. (1988, Table 1).

Unit name	Unit symbol	Area (10^6 km^2)	New global map units (% intersect)
eolian deposits	**Ae**	0.16	**AHtu** (50), **Aa** (32), **lAv** (16)
dune material	**Ad**	0.01	**lNh** (47), **eNh** (27), **HNhu** (11), **Apu** (9), **mNh** (5)
crescentic dune material	**Adc**	0.46	**lHl** (66), **lApd** (18), **Apu** (8), **mAl** (7)
linear dune material	**Adl**	0.23	**lApd** (87), **Apu** (7), **Hpe** (5)
mantle material	**Am**	1.76	**lHl** (50), **mAl** (36), **Hpe** (8)
slide material	**As**	0.62	**lAa** (40), **ANa** (27), **mNh** (5), **AHi** (5)
polar ice deposits	**Api**	0.96	**lApc** (60), **Apu** (21), **lHl** (14)
polar layered deposits	**Apl**	1.84	**Apu** (87), **lApc** (7)
younger channel material	**Ach**	0.01	**mAl** (52), **mNh** (34), **lHl** (8)
older channel material	**Hch**	1.46	**Hto** (29), **Nhu** (27), **mNh** (10), **Ht** (9), **eHt** (6)
younger flood-plain material	**Achp**	0.05	**lAv** (83), **eHt** (11), **HNt** (5)
older flood-plain material	**Hchp**	1.05	**Hto** (40), **Nhu** (22), **lNh** (10), **AHv** (10)
chaotic material	**Hcht**	0.81	**Ht** (66), **HNt** (13), **mNh** (8)
younger channel system material, undivided	**Achu**	0.97	**lAv** (78), **Htu** (5), **AHtu** (5)
tear-drop shaped bar or island	**b**	0.04	**Hto** (40), **Nhu** (32), **AHv** (11), **mNh** (7)
Arcadia Formation, member 5	**Aa_5**	0.21	**Av** (37), **lAv** (29), **lHt** (21), **lHl** (11)
Arcadia Formation, member 4	**Aa_4**	0.67	**Av** (58), **lAv** (36)
Arcadia Formation, member 3	**Aa_3**	1.74	**lAv** (67), **Av** (16), **AHv** (11)
Arcadia Formation, member 2	**Aa_2**	0.14	**Av** (56), **lHl** (40)
Arcadia Formation, member 1	**Aa_1**	3.94	**lHl** (47), **lHt** (17), **eHt** (7), **AHv** (7), **Hto** (6), **HNt** (6)
Medusae Fossae Formation, upper member	**Amu**	1.00	**AHtu** (94)
Medusae Fossae Formation, middle member	**Amm**	0.89	**AHtu** (63), **Htu** (19), **HNt** (6), **lHt** (5)
Medusae Fossae Formation, lower member	**Aml**	0.61	**AHtu** (53), **Htu** (33), **HNt** (7)
Vastitas Borealis Formation, mottled member	**Hvm**	3.27	**lHl** (79), **mAl** (17)
Vastitas Borealis Formation, grooved member	**Hvg**	2.10	**lHl** (88), **mAl** (8)
Vastitas Borealis Formation, ridged member	**Hvr**	1.38	**lHl** (94)
Vastitas Borealis Formation, knobby member	**Hvk**	5.93	**lHl** (84), **mAl** (10), **AHi** (5)
smooth plains material	**Aps**	2.51	**lHl** (24), **lHt** (19), **AHv** (13), **eHt** (11), **lAv** (8), **eHv** (6), **AHi** (6), **mAl** (5)
etched plains material	**AHpe**	0.47	**eHt** (87), **HNt** (5)
Elysium Formation, member 4	**Ael_4**	0.06	**Av** (77), **eAb** (9), **AHv** (9)
Elysium Formation, member 3	**Ael_3**	1.33	**Av** (58), **eAb** (31)
Elysium Formation, member 2	**Ael_2**	0.09	**Hve** (91), **lHvf** (5)
Elysium Formation, member 1	**Ael_1**	2.58	**AHv** (78), l**Av** (9)
Albor Tholus Formation	**AHat**	0.02	**Hve** (96)
Hecates Tholus Formation	**Hhet**	0.03	**Hve** (95)
Syrtis Major Formation	**Hs**	1.35	**eHv** (95)
dome	**d**	0.01	**mAl** (69), **Hpe** (27)
Olympus Mons Formation, plains member	**Aop**	0.45	**lAv** (71), **AHv** (9), **lAvf** (8), **AHtu** (6)
Olympus Mons Formation, shield member	**Aos**	0.38	**Ave** (93)
Olympus Mons Formation, aureole member 4	**Aoa_4**	0.24	**Aa** (100)
Olympus Mons Formation, aureole member 3	**Aoa_3**	0.13	**Aa** (96)
Olympus Mons Formation, aureole member 2	**Aoa_2**	0.08	**Aa** (91), **lAvf** (5)
Olympus Mons Formation, aureole member 1	**Aoa_1**	0.47	**Aa** (86), **AHtu** (13)
Tharsis Montes Formation, member 6	**At_6**	0.67	**AHv** (91), **lAvf** (7)
Tharsis Montes Formation, member 5	**At_5**	2.99	**AHv** (92)
Tharsis Montes Formation, member 4	**At_4**	1.21	**AHv** (94)
Tharsis Montes Formation, member 3	**AHt_3**	1.23	**AHv** (63), **Ave** (25)
Tharsis Montes Formation, member 2	**Ht_2**	0.62	**AHv** (88), **lHvf** (5)
Tharsis Montes Formation, member 1	**Ht_1**	0.18	**AHv** (89), **AHi** (8)
Alba Patera Formation, upper member	**Aau**	0.19	**Ave** (65), **AHv** (35)
Alba Patera Formation, middle member	**Aam**	1.00	**AHv** (100)
Alba Paterae, lower member	**Hal**	1.90	**AHv** (92)
Ceraunius Fossae Formation	**AHcf**	0.47	**AHv** (73), **lAv** (8), **lAvf** (7), **lHvf** (7)
Syria Planum Formation, upper member	**Hsu**	1.35	**lHv** (63), **AHv** (14), **lHvf** (9), **eHv** (8)
Syria Planum Formation, lower member	**Hsl**	0.59	**lHv** (81), **eHv** (16)
Hellas assemblage, knobby plains floor unit	**Ah_8**	0.12	**lHb** (98)
Hellas assemblage, rugged floor unit	**Ah_7**	0.09	**HNb** (44), **mNh** (33), **lNv** (14), **eAb** (8)
Hellas assemblage, reticulate floor unit	**Ah_6**	0.03	**HNb** (95), **eAb** (5)
Hellas assemblage, channeled plains rim unit	**Ah_5**	0.46	**Nhu** (47), **lNh** (28), **eHv** (20),
Hellas assemblage, lineated floor unit	**Ah_4**	0.04	**lHb** (95), **eHb** (5)
Hellas assemblage, dissected floor unit	**Hh_3**	0.76	**lHb** (83), **eHb** (11)
Hellas assemblage, ridged plains floor unit	**Hh_2**	0.81	**eHb** (37), **HNb** (21), **lHb** (16), **lNv** (13)
Hellas assemblage, basin-rim unit	**Nh_1**	1.88	**eNhm** (69), **mNh** (15), **eNh** (8)
Valles Marineris interior deposits, floor material	**Avf**	0.21	**lHt** (32), **Hhu** (25), **Nhu** (16), **Ht** (14), **Aa** (11)
Valles Marineris interior deposits, layered material	**Hvl**	0.09	**Hhu** (86), **Nhu** (7), **lHt** (5)
Tyrrhena Patera Formation	**AHt**	0.05	**Nve** (90), **eHv** (10)
Apollinaris Patera Formation	**AHa**	0.06	**Nve** (46), **Hve** (34), **HNt** (12)
Hadriaca Patera Formation	**AHh**	0.12	**Hve** (75), **eHv** (27)
Amphitrites Formation, patera member	**Hap**	0.12	**lNv** (77), **Nve** (23)
Amphitrites Formation, dissected member	**Had**	0.48	**lNv** (89), **Nve** (9)
Tempe Terra Formation, upper member	**Htu**	0.22	**eHv** (46), **lHvf** (31), **lNh** (7), **eHh** (6)
Tempe Terra Formation, middle member	**Htm**	0.21	**eHv** (50), **lHv** (19), **lHvf** (13), **AHv** (6)
Tempe Terra Formation, lower member	**Htl**	0.04	**mNh** (56), **lHvf** (21), **eHv** (16), **AHi** (8)
Dorsa Argentea Formation, upper member	**Hdu**	0.84	**Hp** (78), **Apu** (7)

Table 4 (*continued*)

Unit name	Unit symbol	Area (10^6 km^2)	New global map units (% intersect)
Dorsa Argentea Formation, lower member	**Hdl**	0.49	**Hp** (52), **lNh** (14), **mNh** (12), **Ap** (11), **Apu** (5)
plateau sequence, smooth unit	**Hpl_3**	3.66	**lNh** (37), **mNh** (18), **eHv (13), mNhm** (8), **AHi** (5)
plateau sequence, mottled smooth plains unit	**Hplm**	0.30	**lNh** (43), **mNh** (25), **eNh** (23)
plateau sequence, subdued cratered unit	**Npl_2**	8.24	**mNh** (56), **lNh** (12), **eNh** (8), H**Nhu** (6), **AHi** (5)
plateau sequence, cratered unit	**Npl_1**	18.54	**mNh** (56), **eNh** (28), **AHi** (7)
plateau sequence, dissected unit	**Npld**	13.38	**mNh** (53), **eNh** (32)
plateau sequence, etched unit	**Nple**	2.59	**mNh** (50), **eNh** (23), **HNb** (6), **AHi** (5)
plateau sequence, ridged unit	**Nplr**	4.61	**mNh** (53), **eNh** (25), **lNh** (13)
plateau sequence, hilly unit	**Nplh**	2.61	**mNhm** (41), **eNh** (24), **mNh** (19), **AHi** (5)
Dorsa Argentea Formation, upper member	**Hf**	1.23	**lHv** (28), **mNh** (10), **eHh** (9), **lNh** (6), **AHi** (5), **Nhu** (5)
highly-deformed terrain materials, older fractured material	**Nf**	1.52	**mNh** (26), **eHv** (19), **lNh** (17), **lHv** (14), **AHv** (5), **Nhu** (5), **eHh** (5), **eNh** (5)
highly-deformed terrain materials, basement complex	**Nb**	0.29	**mNh** (38), **eNh** (25), **AHv** (8), **Nhe** (8), **Nhu** (7), **lNh** (6)
undivided material	**HNu**	3.21	**HNt** (44), **Nhu** (10), **eHt** (8), **lHl** (6), **mAl** (5)
volcano, relative age unknown	**v**	0.31	**Hve** (31), **eHv** (19), **Nhe** (14), **mNh** (12), **eNh** (10), **AHv** (6)
mountainous material	**Nm**	0.36	**eNhm** (61), **eHv** (7), **eNh** (6), **mNhm** (5)
mountain, relative age unknown	**m**	0.03	**eNh** (68), **mNh** (11), **lNh** (9), **AHv** (8)
knobby plains material	**Apk**	2.67	**lHl** (35), **mAl** (16), **eHt** (14), **HNt** (14), **lHt** (10)
ridged plains material	**Hr**	13.56	**mNh** (19), **eHv** (18), **lNh** (18), **eHt** (11), **eHh** (9), **lNv** (8)
impact crater material, superposed	**cs**	3.45	**AHi** (81), **mNh** (7)
impact crater material, partly buried	**cb**	1.32	**eNh** (44), **mNh** (28), **AHi** (11), **lNh** (10)
impact crater material, smooth floor	**s**	1.01	**eNh** (31), **lNh** (22), **mNh** (17), **AHi** (13)

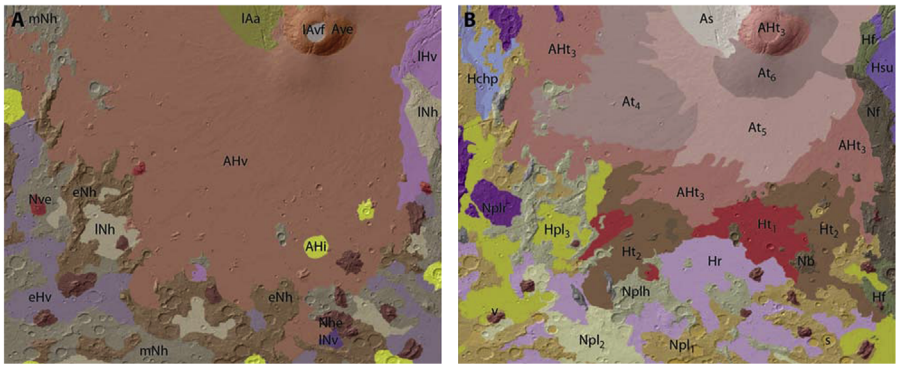

Fig. 3. Daedalia Planum on Mars showing geologic map units of (A) Tanaka et al. (in review) and (B) Scott and Tanaka (1986), as adjusted by Skinner et al. (2006). Superposed on shaded-relief MOLA digital elevation model (128 pixels/degree); scene width ~2400 km.

geologic activity, such as Mars, the fresh crater distribution is a likely indicator of volcanic and eolian erosion/modification efficiency across the planet. They found that younger terrain did generally contain a higher number density of minimally eroded impact craters relative to older terrain, although Hesperian surfaces best preserved original impact morphology. Visible ejecta blanket preservation states on the other hand, far from being uniform across the planet or reflecting the minimally eroded crater distribution, were instead found to strongly be a function of terrain age, where the Noachian terrain had many more craters per unit area with ejecta than did Amazonian terrain. They concluded that crater ejecta blankets may be stable over the course of several billion years on the planet.

With the revised maps and crater and ejecta morphology determined now down to $D \geq 3$ km, we re-examine those analyses here, looking separately at the distribution of 6285 minimally eroded (pristine) morphology craters and 24,893 with preserved ejecta blankets, representing factors of 2.5 and 2.1 increases, respectively, in the number of craters analyzed for this work (Table 5; "minimally eroded" here refers to those craters with a preservation class of 4, based on the occurrence of relatively sharp and high-relief rims, high degrees of ejecta preservation, minimal infilling, and depth/diameter ratios within the upper quartile for craters of that diameter as defined in Robbins and Hynek (2012a)). Due to the smaller minimum crater diameter in the current versus previous studies (3 and 5 km, respectively), a scale factor must be determined and applied to compare the numerical values. This scaling is determined by the ratio of the overall number densities. Here, the number of minimally eroded craters per 10^6 km^2 is 43.5, while the value from Robbins and Hynek (2012b) is 18.9; the scaling is thus 2.3×. The number of radial ejecta craters per 10^6 km^2 in this study is 172.4, and the number in the previous study is 90.2, so the scaling factor is 1.9×.

A total population of 78,073 in the current database have their preservation state and ejecta form classified. For this analysis, the units of the new map were first combined into Amazonian (10% surface area), Hesperian (27%), and Noachian (44%) Periods; most units comprising two periods were not included in the analysis. The latter units constitute 19% of the surface area of the planet, and the Amazonian and Hesperian volcanic unit (AHv) comprises nearly half of it (9%). While the other dual-period units were not considered in this analysis in order to restrict it to the major periods, unit AHv was included and treated separately, because it accounts for a large fraction of the overall surface area of Mars. Map units not included in this crater morphology analysis were: ANa (0.2% surface area), AHtu (1.5%), HNt (2.0%), AHi (5.4%), and HNb (0.4%).

First, we examine the relative densities of minimally eroded craters on terrains by age. While the diameter range of these

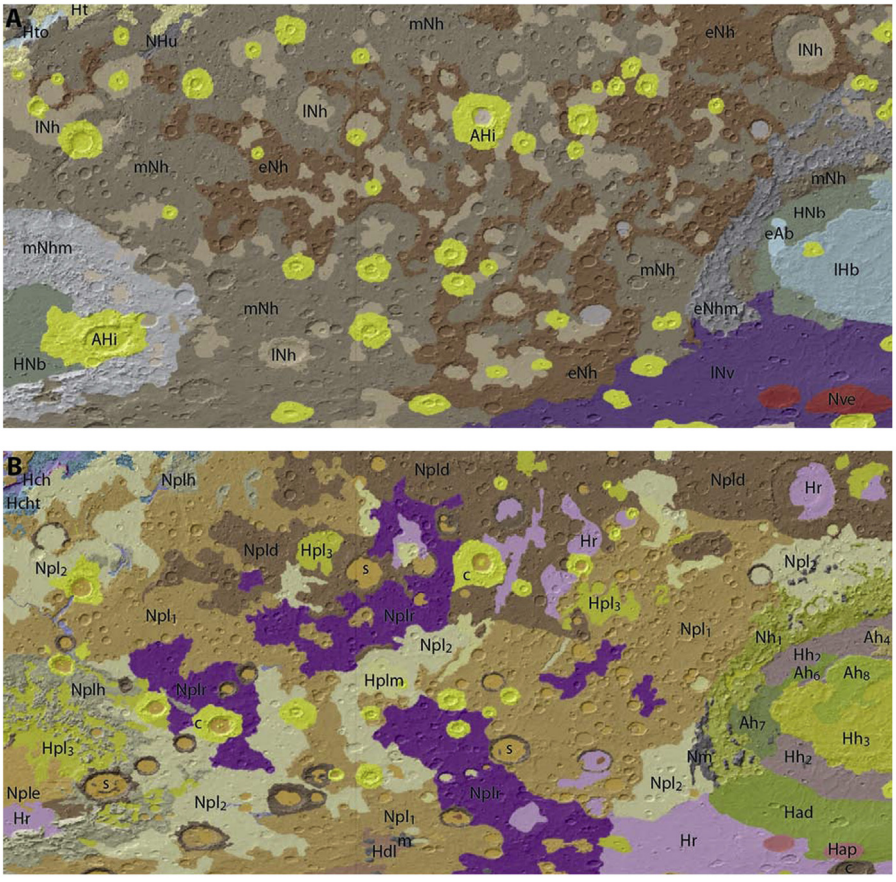

Fig. 4. Noachis Terra region on Mars showing geologic map units of (A) Tanaka et al. (in review) and (B) Scott and Tanaka (1986), Greeley and Guest (1987), and Tanaka and Scott (1987), as adjusted by Skinner et al. (2006). Superposed on shaded-relief MOLA digital elevation model (128 pixels/degree); scene width ~2400 km.

Table 5
Crater morphology statistics on the variously dated terrains (AHv = Amazonian-Hesperian volcanic unit, A = area). First line is the number, second line is number density (per 10^6 km^2) while uncertainty is standard Poisson uncertainty. (Terrain mapping based on a preliminary version of the global map of Mars.)

Terrain	Minimally eroded craters	Degraded craters	Radial/ballistic craters	Lobate ejecta (LE) craters	No ejecta craters	All classified $D \geq 3$ km craters
Global ($A = 144{,}373{,}545$ km^2)	6285 43.5 ± 0.5	28,897 200.2 ± 1.2	24,893 172.4 ± 1.1	18,796 130.2 ± 0.9	34,384 238.2 ± 1.3	78,073 540.8 ± 1.9
Amazonian ($A = 14{,}507{,}516$ km^2)	176 12.1 ± 0.9	596 41.1 ± 1.7	448 30.9 ± 1.5	769 53.0 ± 1.9	817 56.3 ± 2.0	2034 140.2 ± 3.1
Hesperian ($A = 38{,}979{,}786$ km^2)	2299 59.0 ± 1.2	3031 77.8 ± 1.4	3880 99.5 ± 1.6	5036 129.2 ± 1.8	3795 97.4 ± 1.6	12,711 326.1 ± 2.9
Noachian ($A = 64{,}050{,}256$ km^2)	2718 42.4 ± 0.8	22,850 356.8 ± 2.4	17,738 276.9 ± 2.1	10,663 166.5 ± 1.6	26,429 412.6 ± 2.5	54,830 856.0 ± 3.7
AHv ($A = 13{,}177{,}826$ km^2)	728 55.2 ± 2.0	333 25.3 ± 1.4	687 47.4 ± 2.0	1033 78.4 ± 2.4	598 45.4 ± 1.8	2318 175.9 ± 3.7
Amazonian+AHv	904 32.7 ± 1.1	929 33.6 ± 1.1	1135 41.0 ± 1.2	1802 66.1 ± 1.5	1415 51.1 ± 1.4	4352 157.2 ± 2.4
Hesperian+AHv	3027 58.0 ± 1.1	3364 64.5 ± 1.1	4567 87.6 ± 1.3	6069 116.4 ± 1.5	4393 84.2 ± 1.3	15,029 288.1 ± 2.4

craters spans from 3 to 65 km, 80% are $D < 7.2$ km, 95% are $D < 12.8$ km, and 99% are $D < 23.5$ km. If the distribution of minimally eroded craters were even across the planet, one would expect a number density of 43.5 ± 0.5 per 10^6 km^2. Noachian terrain matches that with a density of 42.4 ± 0.8. Hesperian terrain has an apparent over-abundance of minimally eroded craters, 59.0 ± 1.2, as well as unit AHv at 55.2 ± 2.0. Amazonian terrain, conversely, has a marked deficit of minimally eroded craters at 12.1 ± 0.9 per 10^6 km^2. If unit AHv is included with Amazonian terrain, the density rises to 32.7 ± 1.1 per 10^6 km^2—still below the global mean; if AHv is included with Hesperian terrain, the density is 58.0 ± 1.1.

With the scaling factor applied, the results from Robbins and Hynek (2012b) are 39.9 ± 1.7 per 10^6 km^2 for Amazonian terrain, 57.2 ± 1.7 for Hesperian, and 33.5 ± 1.2 for Noachian. The only consistent results are the number density of minimally eroded craters on Hesperian terrain. Amazonian terrain on the new maps has a marked deficit of these craters compared with the Viking-based maps, although with unit AHv included in the new map's Amazonian terrains the results are consistent within the 2.6–σ level. The Noachian terrain in our work has more minimally eroded craters per area, a result that is suggestive of smaller craters being more likely to form on any given terrain than larger craters being preserved on older terrain.

A decrease in number density of minimally eroded craters on Amazonian versus Hesperian terrains indicates that crater erosion or modification is not strictly related to the length of time a crater exists on a particular surface. We interpret this as differences in the physical character of the impacted materials, i.e., consolidated versus unconsolidated lithic materials being able to withstand erosion. The inclusion of the AHv volcanic unit with the Amazonian acting to increase the number density supports this interpretation, given the increased strength of volcanic material for better preservation of these morphologies. The observation that the Noachian terrain has fewer minimally eroded craters can be interpreted to be the result of one or more factors. One factor may be that minimally eroded crater morphology persisted at least from the Hesperian through the present-day due to a low rate of impact gardening and/or high target material strength. Another possible factor is terrain softening such as by periglacial-type processes that are observed at mid- to high-southern latitudes (Jankowski and Squyres, 1992), which are dominated by the Noachian terrain, modified craters more easily. This activity would have decreased the number observed there relative to Hesperian-mapped surfaces, which in turn decreases the global average. Similarly, a majority of volcanic terrain was classified as Hesperian (or unit AHv) and this terrain type, in general, would likely result in ejecta more resistant to degradation than that of most other terrain types. That is, Hesperian and unit AHv are dominated by material that is more likely to preserve morphologies associated with minimally eroded impact craters. These effects combined may account for the decrease in this type of craters on Noachian relative to Hesperian terrain, and it could account for the increase for such in Hesperian terrain and unit AHv.

Spatial densities of impact craters that are surrounded by well-formed, continuous ejecta blankets similarly serve as a proxy for erosion or modification of particular geologic terrains. There are 24,893 craters in the database with diameters ≥3 km that have only radial (ballistic) ejecta. There are an additional 18,796 craters classified with layered ejecta (LE) blankets (Barlow et al., 2000). While we list the LE numbers in Table 5, interpretation should proceed with caution, as LE craters are highly correlated with terrain type and location. For example, single- and double-layered ejecta blankets are both found primarily between 50°–75°N latitude (and single-layered ejecta also within volcanic terrain, regardless of age) (see Barlow and Perez (2003) and Robbins and Hynek (2012b)). An even distribution of craters with radial ejecta blankets should be 172.4 ± 1.1 craters per 10^6 km^2. Radial-ejecta densities are 47.4 ± 2.0 on unit AHv, 30.9 ± 1.5 on Amazonian terrains, 99.5 ± 1.6 on Hesperian terrains, and 276.9 ± 2.1 on Noachian terrains. Combining Amazonian terrain with unit AHv raises the density to 41.0 ± 1.2, while combining it with Hesperian lowers that to 87.6 ± 1.3. Scaling the Viking results yields densities of 44.0 ± 1.6 on the Amazonian terrain, 103.2 ± 2.0 on the Hesperian, and 307.7 ± 3.3 for the Noachian. These relative densities are consistent with what Robbins and Hynek (2012b) found, and both the Hesperian and Amazonian results are just outside the $1-\sigma$ values if unit AHv is combined with Amazonian terrain. This indicates that there are no significant deviations between densities when using the Viking- or post-Viking maps, except when separating out the AHv unit. These indicate that radial ejecta blankets can be preserved on Mars through significant erosional and resurfacing episodes.

3.5. Resurfacing history as a function of unit type

In the global map, each unit is assigned an age range according to the Martian chronologic periods and epochs (Fig. 1), thereby permitting calculation of the amount of area resurfaced for each time step. However, this approach has limitations. The depth of resurfacing and total volume of material eroded, transported, and/or deposited are not measured. Volumetrically, some materials such as the volcanic edifice units are especially thick and obviously under-represented, whereas units such as polar cap and dune units are over-represented because of their relatively low mean thicknesses. Although Tanaka et al. (1988) estimated the buried areas of units, these values were highly uncertain and thus are not considered in this paper. Similarly, Greeley (1987) estimated volcanic resurfacing through time, but these estimates also are based on largely unconstrained estimates of rock volumes.

Some of the units that we identify and describe in the new global geologic map of Mars span multiple epochs. In order to estimate areal proportions of units per epoch, a constant resurfacing rate for each unit is assumed for the duration of its formation (but actual surface ages within units may be highly complex and skewed, which detailed mapping studies may elucidate). Thus, an Amazonian unit is proportioned into the Early, Middle, and Late epochs according to the estimated durations of each using the Hartmann and Neukum chronology functions (Neukum et al., 2001; Hartmann, 2005) as calculated by Werner and Tanaka (2011). In each of these chronologies, the Early Amazonian Epoch is much longer than the Middle and Late epochs, so that the estimated epoch proportions of an Amazonian unit would be dominated by the Early Amazonian. We then summed the surface coverages by unit group per epoch and chronology function (Tables 6 and 7; Figs. 5 and 6). Given the durations of each epoch, we estimated mean resurfacing rates for both chronology models by epoch (Tables 8 and 9) and mean epoch age (Figs. 7 and 8). These rates provide a summary history for the resurfacing of Mars by terrain and unit types.

A previous reconstruction of resurfacing rates on Mars based on a global map using Viking images (Tanaka et al., 1988) attempted to differentiate the rates by process categories; however, for many units and unit groups, differentiating proportions of units that were formed by particular processes (e.g., volcanism, impact, sedimentation, etc.) is problematic and conjectural. In our

Table 6
Estimated area of resurfacing (in 10^6 km^2) for each Mars global unit group per epoch, based on Hartmann chronology.

Epoch*	Highland	Basin	Transition	Lowland	Polar	Volcanic	Apron	Impact	Total
lA	–	–	0.15	–	2.71	4.68	0.88	0.52	8.94
mA	–	–	0.42	2.99	0.05	3.16	0.80	1.42	8.84
eA	–	0.54	1.37	–	0.16	10.40	0.22	4.68	17.36
lH	0.47	0.91	5.70	15.96	1.06	4.64	–	0.88	29.61
eH	2.00	0.62	4.99	–	0.45	5.88	–	0.37	14.32
lN	9.68	0.37	0.73	–	–	2.33	0.03	–	13.14
mN	34.43	–	0.29	–	–	0.04	0.01	–	34.77
eN	16.96	–	0.37	–	–	0.05	0.01	–	17.40
Total	63.54	2.44	14.01	19.06	4.43	31.18	1.95	7.87	144.37

* A, Amazonian; H, Hesperian; N, Noachian; e, Early; m, Middle; l, Late.

Table 7
Estimated area of resurfacing (in 10^6 km^2) for each Mars global unit group per epoch, based on Neukum chronology.

Epoch*	Highland	Basin	Transition	Lowland	Polar	Volcanic	Apron	Impact	Total
lA	–	–	0.23	–	2.72	5.20	0.73	0.80	9.70
mA	–	–	0.64	2.99	0.07	4.81	0.41	2.24	11.16
eA	–	0.54	1.21	–	0.13	9.10	0.77	4.23	15.98
lH	0.48	0.91	5.29	15.96	1.02	3.76	–	0.40	27.82
eH	2.02	0.65	5.02	–	0.49	5.89	–	0.19	14.26
lN	9.29	0.34	0.54	–	–	2.29	0.01	–	12.47
mN	34.61	–	0.49	–	–	0.06	0.01	–	35.18
eN	17.14	–	0.58	–	–	0.07	0.01	–	17.81
Total	63.54	2.44	14.01	18.95	4.43	31.18	1.95	7.87	144.37

* A, Amazonian; H, Hesperian; N, Noachian; e, Early; m, Middle; l, Late.

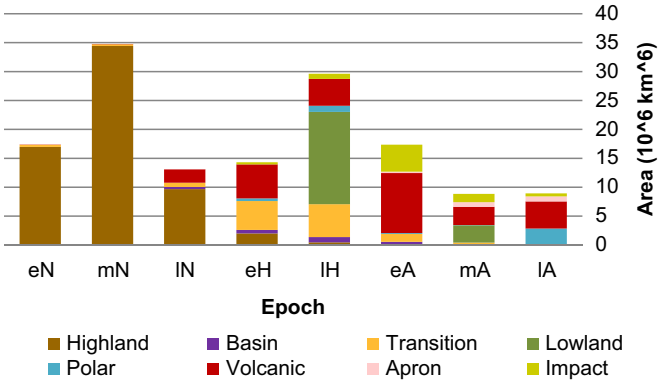

Fig. 5. Resurfaced areas on Mars per unit group and epoch, Hartmann chronology model (A, Amazonian; H, Hesperian; N, Noachian; e, Early; m, Middle; l, Late).

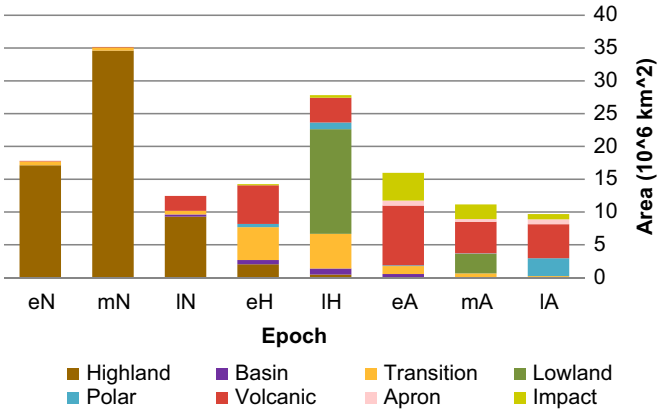

Fig. 6. Resurfaced areas on Mars per unit group and epoch, Neukum chronology model (A, Amazonian; H, Hesperian; N, Noachian; e, Early; m, Middle; l, Late).

unit groups, only the volcanic group and impact unit are explicitly related to a process. To greater or lesser degrees, most units identified and described in the new geologic map originated by multiple and/or uncertain geologic processes. Moreover, impacts and volcanism contributed to the origin of the highland and transitional units, so even the impact and volcanic resurfacing rates are not fully known.

Although both mapping and chronology models have been improved since the Viking-based resurfacing estimates (Tanaka et al., 1988; Hartmann and Neukum, 2001), both show similar overall trends, with highest resurfacing rates in the Middle Noachian and a dip in the Late Noachian followed by a rise during the Hesperian and lowest rates in the Amazonian. Our reconstructions (Tables 8 and 9; Figs. 7 and 8) also indicate rising resurfacing rates from the Early Amazonian to the Late Amazonian by three- to six-fold. We interpret this increase as an effect of: (1) widespread plains volcanism in Amazonis and Elysium Planitiae during the Late Amazonian, (2) under-representation of Early Amazonian surfaces due to their partial burial by Middle and Late Amazonian units, and (3) under-representation of Early Amazonian surfaces in a volumetric sense due to this epoch's much longer duration, and thus the likelihood that its units are much thicker. In summary, the resurfacing rates determined here, although helpful in characterizing relative levels of geologic activity over time, include uncertainties due to both observational biases and methodological limitations. Further detailed mapping and crater population studies can help elucidate and address these problems.

4. Conclusions

The new global map of Mars has been prepared in a digital form suitable for spatial statistical analyses, useful for (1) additional characterization of the map units by mapping other remotely sensed data and (2) spatially based comparisons with other geologic features and with previous mapping results. In this paper, we derived thematic maps of the units by their age and group types, which can also be used for such analyses. We have demonstrated this utility by comparing the geologic mapping with other global thematic maps including elevation and slope data, an impact crater size and morphology inventory, and previous, Viking-based geology. We also have derived a new, generalized resurfacing history for Mars. Principal results include:

1. Construction of a chronostratigraphic map of Mars (Fig. 1) that provides summary dating results based on superposition relationships and crater-density determinations (Table 1) for all mapped outcrops of the 44 units in the new global map of Mars.
2. Derivation of maps showing the distribution of 8 unit groups for the Noachian, Hesperian, and Amazonian Periods (Fig. 2) that illustrate the spatial/temporal/geological resurfacing of Mars. These maps illustrate the dominance of highland surface modification in the Noachian Period; highland modification and lowland and basin fill in the Hesperian Period; and volcanic plains and shield development, polar and localized plains deposition, and scattered impacts in both the Hesperian and Amazonian Periods.
3. Calculation of mean surface elevations and slopes for each unit (Table 2) using the 128 pixel per degree MOLA digital terrain model quantifies how most units reflect their terrain group characteristics. Highland and edifice units have higher mean elevations, whereas lowland and basin units are lowest. Edifice, massif, apron, undivided, and Hesperian transition units tend to be steepest (3° to 7°), whereas lowland and basin units and

Table 8
Estimated resurfacing rates (km^2/yr) per unit group per epoch, based on Hartmann chronology; durations from Werner and Tanaka (2011).

Epoch*	Duration (myr)	Highland	Basin	Transition	Lowland	Polar	Volcanic	Apron	Impact	Total
lA	235	–	–	0.001	–	0.012	0.020	0.004	0.02	0.038
mA	645	–	–	0.001	0.005	–	0.005	0.001	0.02	0.014
eA	2120	–	–	0.001	–	–	0.005	–	0.02	0.008
lH	400	0.001	0.002	0.014	0.040	0.003	0.012	–	0.02	0.074
eH	170	0.012	0.004	0.029	–	0.003	0.035	–	0.02	0.084
lN	280	0.035	0.001	0.003	–	–	0.008	–	–	0.047
mN	110	0.313	–	0.003	–	–	–	–	–	0.316
eN	140	0.121	–	0.003	–	–	–	–	–	0.124

* A, Amazonian; H, Hesperian; N, Noachian; e, Early; m, Middle; l, Late.

Table 9
Estimated resurfacing rates (km^2/yr) per unit group per epoch, based on Neukum chronology; durations from Werner and Tanaka (2011).

Epoch*	Duration (myr)	Highland	Basin	Transition	Lowland	Polar	Volcanic	Apron	Impact	Total
lA	387	–	–	0.001	–	0.007	0.013	0.002	0.02	0.025
mA	1063	–	–	0.001	0.003	–	0.005	–	0.02	0.010
eA	2010	–	–	0.001	–	–	0.005	–	0.02	0.008
lH	190	0.003	0.005	0.028	0.084	0.005	0.020	–	0.02	0.146
eH	90	0.022	0.007	0.056	–	0.005	0.065	–	0.02	0.158
lN	120	0.077	0.003	0.004	–	–	0.019	–	–	0.104
mN	110	0.315	–	0.004	–	–	0.001	–	–	0.320
eN	130	0.132	–	0.004	–	–	0.001	–	–	0.137

* A, Amazonian; H, Hesperian; N, Noachian; e, Early; m, Middle; l, Late.

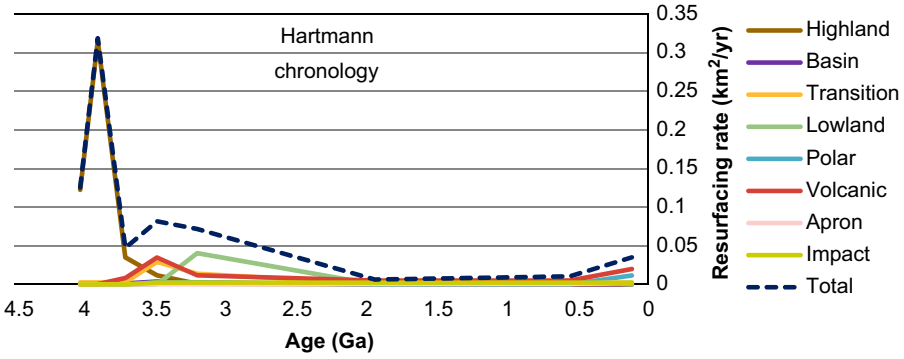

Fig. 7. Resurfacing rates on Mars per unit group and mean age of epoch, the Hartmann chronology model.

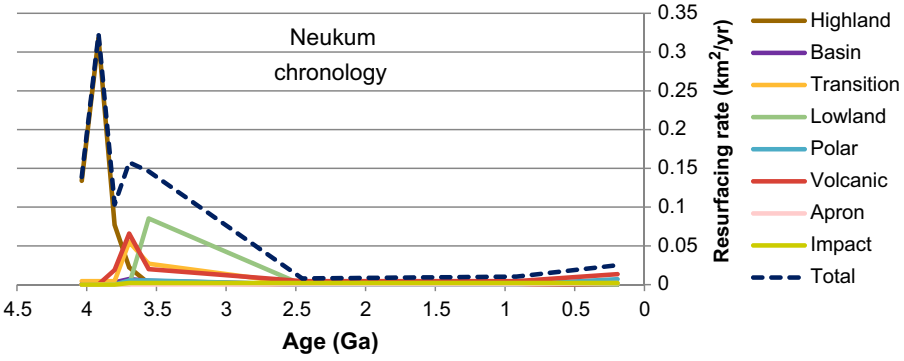

Fig. 8. Resurfacing rates on Mars per unit group and mean age of epoch, the Neukum chronology model.

some others of Amazonian to Hesperian age are relatively flat ($<1^\circ$).

4. Comparisons of the new map units with those of the Viking-based global map series (Figs. 3 and 4; Tables 3 and 4) show that post-Viking map bases, new global mapping approaches and methods, detailed and global crater dating techniques, and other data sets and studies have resulted in major updates and qualitative and quantitative improvements in how surfaces are characterized by the new global mapping. In particular, many highlands areas are now understood to be an epoch or two older than previously recognized. Also, much of the Tharsis lava plains are currently more conservatively mapped than in the Viking maps given that age relations are now recognized to be more complex.

5. Analysis of crater morphology statistics (Table 5) for diameters ≥3 km using the current map largely agrees with results for diameters ≥5 km using the Viking-based map. There are relatively high densities of minimally eroded craters on Hesperian versus Noachian surfaces, likely the result of higher proportions of more erosionally resistant of volcanic rocks in the former.
6. Determination of resurfacing areas and rates for unit groups by epoch (Figs. 5–8; Tables 6–9), even when considering how the data are biased toward younger units and are otherwise skewed, show how resurfacing rates on Mars have decreased dramatically particularly from the Middle Noachian Epoch (~3.8 Ga) to the beginning of the Amazonian Period (~2–2.5 Ga). However, resurfacing by volcanic, polar, lowland, and apron units shows moderate resurgence in the Middle and Late Amazonian Epochs, but may result from observational bias.

Acknowledgments

Constructive comments by Monica Pondrelli and Larry Crumpler improved the manuscript. Ross Irwin, James Dohm, Eric Kolb, Thomas Platz, and Greg Michael contributed to the geologic mapping and associated crater dating upon which this analysis is based. A grant from the NASA Planetary Geology and Geophysics Program funded this research.

References

Barlow, N.G., 1988. Crater size-frequency distributions and a revised Martian relative chronology. Icarus 75, 285–305, http://dx.doi.org/10.1016/0019-1035(88)90006-1.

Barlow, N.G., Perez, C.B., 2003. Martian impact crater ejecta morphologies as indicators of the distribution of subsurface volatiles. Journal of Geophysical Research 108 (E8), 5085, http://dx.doi.org/10.1029/2002JE002036.

Barlow, N.G., Boyce, J.M., Costard, F.M., Craddock, R.A., Garvin, J.B., Sakimoto, S.E.H., Kuzmin, R.O., Roddy, D.J., Soderblom, L.A., 2000. Standardizing the nomenclature of Martian impact crater ejecta morphologies. Journal of Geophysical Research 105 (E11), 26,733–26,738, http://dx.doi.org/10.1029/2000JE001258.

Burr, D.M., Enga, M.-T., Williams, R.M.E., Zimbelman, J.R., Howard, A.D., Brennand, T. A., 2009. Pervasive aqueous paleoflow features in the Aeolis/Zephyria Plana region, Mars. Icarus 200, 52–76, http://dx.doi.org/10.1016/j.icarus.2008.10.014.

Bouysee, Ph., 2009. Geological map of the world at 1:50,000,000 (Third Edition): Commission for the Geological Map of the World, Paris, France, scale 1:50,000,000.

Christensen, P.R., Jakosky, B.M., Kieffer, H.H., Malin, M.C., McSween Jr., H.Y., Nealson, K., Mehall, G.L., Silverman, S.H., Ferry, S., Caplinger, M., M., Ravine, 2004. The Thermal emission Imaging System (THEMIS) for the Mars 2001 Odyssey Mission. Space Science Reviews 110, 85–130.

Edwards, C.S., Nowicki, K.J., Christensen, P.R., Hill, J., Gorelick, N., Murray, K., 2011. Mosaicking of global planetary image datasets: 1. Techniques and data processing for Thermal Emission Imaging System (THEMIS) multi-spectral data. Journal of Geophysical Research 116, E10008, http://dx.doi.org/10.1029/2010JE003755.

Greeley, R., Guest, J.E., 1987. Geologic map of the eastern equatorial region of Mars. United States Geological Survey Miscellaneous Investigations Series. (Map I-1802-B, scale 1:15,000,000).

Greeley, R., 1987. Release of juvenile water on Mars: estimated amounts and timing associated with volcanism. Science 236, 1653–1654.

Hartmann, W.K., 2005. Martian cratering 8: isochron refinement and the chronology of Mars. Icarus 174 (2), 294–320.

Hartmann, W.K., Neukum, G., 2001. Cratering chronology and the evolution of Mars. Space Science Reviews 96, 165–194.

Ivanov, B.A., 2001. Mars/Moon cratering rate ratio estimates. Space Science Reviews 96, 87–104.

Jankowski, D.G., Squyres, S.W., 1992. Topography of impact craters in "softened" terrain on Mars. Icarus 100, 26–39, http://dx.doi.org/10.1016/00191035(92)90015-Y.

Kneissl, T., van Gasselt, S., Neukum, G., 2011. Map-projection-independent crater size-frequency determination in GIS environments: new software tool for ArcGIS. Planetary and Space Science 59 (11–12), 1243–1254, http://dx.doi.org/10.1016/j.pss.2010.03.015.

Kreslavsky, M.A., Head III, J.W., 2000. Kilometer-scale roughness of Mars: results from MOLA data analysis. Journal of Geophysical Research 105 (E11), 26,695–26,711.

Michael, G.G., Neukum, G., 2010. Earth and Planetary Science Letters 294, 223–229, http://dx.doi.org/10.1016/j.epsl.2009.12.041.

Neukum, G., Ivanov, B.A., Hartmann, W.K., 2001. Cratering records in the inner solar system in relation to the lunar reference system. Space Science Reviews 96, 55–86.

Neumann, G.A., Rowlands, D.D., Lemoine, F.G., Smith, D.E., Zuber, M.T., 2001. Crossover analysis of Mars Orbiter Laser Altimeter data. Journal of Geophysical Research 106 (E10), 23,753–23,768.

Platz, T., Michael, G.G., Tanaka, K.L., Skinner, J.A., Jr., Kneissl, T., Fortezzo, C.M. Crater-based dating of geological units on Mars: methods and application for the new global geological map. Icarus 225, 806–827, http://dx.doi.org/10.1016/j.icarus.2013.04.021.

Reed, Jr., J.C., Wheeler, J.O., Tucholke, B.E., compilers, 2005. Geologic Map of North America: Continent—Scale Map—001, Geological Society of America, Boulder, Colorado, scale 1:5,000,000.

Robbins, S.J., Hynek, B.M., 2012a. A new global database of Mars impact craters ≥1 km: 1. Database creation, properties, and parameters. Journal of Geophysical Research 117, E05004, http://dx.doi.org/10.1029/2011JE003966.

Robbins, S.J., Hynek, B.M., 2012b. A new global database of Mars impact craters ≥1 km: 2. Global crater properties and regional variations of the simple-to-complex transition diameter. Journal of Geophysical Research 117, E06001, http://dx.doi.org/10.1029/2011JE003967.

Scott, D.H., Carr, M.H., 1978. Geologic map of Mars. United States Geological Survey Misc. Invest. Ser.. (Map I-1083, scale 1:25,000,000).

Scott, D.H., Tanaka, K.L., 1986. Geologic map of the western equatorial region of Mars. United States Geological Survey Misc. Invest. Ser. (Map I-1802-A, scale 1:15,000,000).

Seidelmann, P.K., Abalakin, V.K., Bursa, M., et al., 2002. Report of the IAU/IAG working group on cartographic coordinates and rotational elements of the planets and satellites—2000. Celestial Mechanics and Dynamical Astronomy 82, 83–110.

Skinner Jr., J.A., Fortezzo, C.M., 2013. The role of photogeologic mapping in traverse planning: Lessons from DRATS 2010 activities: ActaAstronautica, 90 (2), 242–263, http://dx.doi.org/10.1016/j.actaastro.2011.11.011.

Skinner Jr., J.A., Hare, T.M., Tanaka, K.L., 2006. Digital renovation of the Atlas of Mars 1:15,000,000-scale global Geologic Series maps. Lunar and Planetary Science Conference 37 #2331 (abstract) (online).

Skinner Jr., J.A., Tanaka, K.L., Platz, T., 2012. Widespread loess-like deposit in the Martian northern lowlands identifies Middle Amazonian climate change. Geology 40, 1127–1130, http://dx.doi.org/10.1130/G33513.1.

Smith, D.E., Zuber, M.T., Frey, H.V., et al., 2001. Mars Orbiter Laser Altimeter: experiment summary after the first year of global mapping of Mars. Journal of Geophysical Research 106 (E10), 23,689–23,722.

Tanaka, K.L., 1986. The stratigraphy of Mars. Journal of Geophysical Research 91 (Suppl. B13), E139–158.

Tanaka, K.L., Fortezzo, C.M., 2012. Geologic map of the north polar region of Mars. United States Geological Survey Sci. Invest. (Map SIM-3177, scale 1:2,000,000).

Tanaka, K.L., Scott, D.H., 1987. Geologic map of the polar regions of Mars. United States Geological Survey Misc. Invest. Ser.. (Map I-1802-C, scale 1:15,000,000).

Tanaka, K.L., Isbell, N.K., Scott, D.H., Greeley, R., Guest, J.E., 1988. The resurfacing history of Mars: a synthesis of digitized, Viking-based geology. Lunar and Planetary Science Conference 18, 665–678.

Tanaka, K.L., Skinner Jr., J.A., Hare, T.M., 2005. Geologic map of the northern plains of Mars. United States Geological Survey Sci. Invest. (Map SIM-2888, scale 1:15,000,000).

Tanaka, K.L., Skinner Jr., J.A., Crumpler, L.S., Dohm, J.M., 2009. Assessment of planetary geologic mapping techniques for Mars using terrestrial analogs: the SP Mountain area of the San Francisco Volcanic Field, Arizona. Planetary and Space Science 57, 510–532, http://dx.doi.org/10.1016/j.pss.2008.06.012.

Tanaka, K.L., Skinner, J.A., Jr., Dohm, J.M., Irwin, R.P., III, Kolb, E.J., Fortezzo, C.M., Platz, T., Michael, G., Hare, T.M. Geologic map of Mars. United States Geological Survey Sci. Invest. (Map, scale 1:20,000,000) (in review).

Werner, S.C., Tanaka, K.L., 2011. Redefinition of the crater-density and absolute-age boundaries for the chronostratigraphic system of Mars. Icarus 215, 603–607, http://dx.doi.org/10.1016/j.icarus.2011.07.024.